Nano Research 2016, 9(11): 3494–3503
DOI 10.1007/s12274-016-1226-3
Research Article
ISSN 1998-0124
CN 11-5974/O4

Hollow PtNi alloy nanospheres with enhanced activity and methanol tolerance for the oxygen reduction reaction

Huimin Liu[1,§], Xinyu Liu[2,§], Yumei Li[1], Yufeng Jia[2], Yawen Tang[2] (✉), and Yu Chen[1] (✉)

[1] *Key Laboratory of Macromolecular Science of Shaanxi Province, School of Materials Science and Engineering, Shaanxi Normal University, Xi'an 710062, China*
[2] *Jiangsu Key Laboratory of New Power Batteries, Jiangsu Collaborative Innovation Center of Biomedical Functional Materials, School of Chemistry and Materials Science, Nanjing Normal University, Nanjing 210023, China*
[§] *These authors contributed equally to this work.*

Received: 12 May 2016
Revised: 4 July 2016
Accepted: 21 July 2016

KEYWORDS
cyanogel,
PtNi alloy,
chemical functionalization,
oxygen reduction reaction,
methanol tolerance

ABSTRACT

The development of active and methanol-tolerant cathode electrocatalysts for the oxygen reduction reaction (ORR) is extremely important for accelerating the commercial viability of direct methanol fuel cells (DMFCs). In this work, we present an efficient and template-free route for facile synthesis of cyanide (CN^-)-functionalized PtNi hollow nanospheres (PtNi@CN HNSs) with a high alloying degree using a simple cyanogel reduction method at room temperature. The physical and electrocatalytic properties of the PtNi@CN HNSs were investigated by various physical and electrochemical techniques. The PtNi@CN HNSs exhibited significantly enhanced electrocatalytic activity, durability, and particular methanol tolerance for the ORR as compared to commercial Pt black, and thus they are promising cathode electrocatalysts for DMFCs.

1 Introduction

Direct methanol fuel cells (DMFCs) may be a highly promising power source for portable electronic devices and automobiles owing to their high energy efficiency, convenient storage and transportation, and relatively clean utilization [1–8]. However, the development of DMFCs suffers from high cost and low oxygen reduction reaction (ORR) kinetics of cathode Pt electrocatalysts. Recent reports have demonstrated that alloying Pt with Ni not only significantly enhances the ORR activity owing to the reduction in the Pt–Pt bond distance and the shift of the Pt d-band center but also improves the utilization of cathode Pt electrocatalysts [9–25]. For example, both octahedral Pt_1Ni_1 alloy nanoparticles and hollow Pt_5Ni_1 alloy nanoparticles have exhibited higher mass activity and specific activity as compared to Pt/C electrocatalysts [24, 25]. However, PtNi alloy nanocrystals are also highly active for the methanol oxidation reaction (MOR)

Address correspondence to Yu Chen, ndchenyu@gmail.com; Yawen Tang, tangyawen@njnu.edu.cn

because of the bifunctional mechanism [26–34]. As a result, because of the methanol crossover problem, the competitive reaction between the ORR and the MOR at the cathode inevitably decreases the performance of DMFCs. Thus, improving the ORR selectivity of PtNi alloy nanocrystals is still very necessary.

Recently, functionalizing noble metal nanocrystals with inorganic or organic ligands have become an effective strategy for achieving selectivity owing to the steric and hydrophilic/hydrophobic effects of ligands [35–48]. For example, cyanide (CN^-)-modified Pt electrocatalysts displayed significantly enhanced ORR activity in an H_2SO_4 solution as compared to the naked Pt electrocatalysts by suppressing the adsorption of SO_4^{2-} ions [35, 36]. In one study, calix[4]arene self-assembled monolayer-modified Pt electrocatalysts selectively blocked the ORR but retained their high activity for the hydrogen oxidation reaction owing to an ensemble effect [37, 38]. In another study, polyallylamine-modified Pt nanocrystals displayed the particular alcohol tolerance for the ORR by preventing the diffusion of alcohol molecules from water to the underlying Pt owing to the steric effect and alcohol-phobic property of the polyallylamine layers [46–48].

In this work, we report a facile cyanogel reduction strategy [49–53] to synthesize cyanide (CN^-)-functionalized hollow PtNi nanospheres (PtNi@CN HNSs) with a high alloying degree. In brief, PtNi@CN HNSs were readily obtained by reducing potassium tetrachloroplatinate(II) (K_2PtCl_4)/potassium tetracyanonicolate(II) ($K_2Ni(CN)_4$) cyanogel (Fig. S1 in the Electronic Supplementary Material (ESM)) with $NaBH_4$ solution under strong stirring. The as-prepared PtNi@CN HNSs exhibited high activity and particular methanol tolerance for the ORR.

2 Experimental

2.1 Reagents and chemicals

Analytical reagent-grade K_2PtCl_4, $K_2Ni(CN)_4$, sodium borohydride ($NaBH_4$), methanol (CH_3OH), perchloric acid ($HClO_4$), and sulfuric acid (H_2SO_4) were purchased from Sinopharm Chemical Reagent Co., Ltd. (Shanghai, China). Commercial Pt black was purchased from Johnson Matthey Corporation (Ravenna, OH, USA).

2.2 Preparation of PtNi@CN HNSs

In a typical synthesis, 4 mL of 0.15 M K_2PtCl_4 and 2 mL of 0.15 M $K_2Ni(CN)_4$ aqueous solutions were mixed and stirred for 10 min. Then, the mixture was heated at 95 ℃ for 24 h to generate the pale green K_2PtCl_4/$K_2Ni(CN)_4$ cyanogel (Fig. S1 in the ESM). After cooling to room temperature, 10 mL of a 0.1 $g \cdot mL^{-1}$ $NaBH_4$ solution was added to the pale green K_2PtCl_4/$K_2Ni(CN)_4$ cyanogel under strong stirring. Then, PtNi@CN HNSs were collected by centrifugation at 10,000 rpm for 25 min, washed with 0.1 M $HClO_4$ solution and Millipore water successively, and then dried at 60 ℃ in a vacuum dryer for 12 h.

2.3 Physical characterization

Transmission electron microscopy (TEM) measurements were carried out using a JEOL JEM-2100F TEM system. Energy dispersive X-ray (EDX) maps were carried out using a JEOL JSM-7600F scanning electron microscope. EDX analysis was performed using a JSM-2010 field-emission scanning electron microscope. X-ray diffraction (XRD) patterns were obtained with a Model D/max-rC X-ray diffractometer using a Cu Kα radiation source. High-resolution X-ray photoelectron spectroscopy (XPS) measurements were carried out using a Thermo VG Scientific ESCALAB 250 spectrometer. The binding energy was calibrated by means of the C 1s peak energy of 284.6 eV. Fourier transform infrared (FT-IR) analysis was performed using a Bruker Tensor 27 spectrometer. Dynamic light scattering (DLS) measurements were performed using a Malvern Zetasizer Nano ZS90 system.

2.4 Electrochemical measurements

All electrochemical experiments were performed in an all-Teflon three-electrode cell by using a CHI 660 C electrochemical analyzer (CH Instruments, Shanghai, Chenghua Co.) with a Gamry RDE710 rotating disk electrode at 30 ± 1 ℃. A platinum wire acted as the auxiliary electrode, a saturated calomel electrode (SCE) acted as the reference electrode, and a catalyst-modified glassy carbon electrode worked as the working electrode. All potentials in this study are

reported with respect to the reversible hydrogen electrode (RHE). Working electrodes were prepared according to the previously reported procedure [54]. Typically, the electrocatalyst ink was obtained by ultrasonic mixing of 10 mg of electrocatalyst and 5 mL of isopropanol/Nafion® solution (20% isopropanol and 0.02% Nafion®) for 60 min. Then, 20 μL of the electrocatalyst ink was drop coated onto a polished glassy carbon electrode and dried at room temperature.

3 Results and discussion

3.1 Sample characterization

EDX measurements were conducted to detect the bulk chemical composition of the PtNi@CN HNSs (Fig. 1(a)). The Pt/Ni atomic ratio (70:30) in the PtNi@CN HNSs was slightly greater than the Pt/Ni stoichiometric ratio in the $K_2PtCl_4/K_2Ni(CN)_4$ cyanogel (2:1), which may have been the result of the dissolution of un-alloyed Ni during $HClO_4$ washing of the products. XPS was performed to investigate the surface chemical composition of the PtNi@CN HNSs (Fig. S2 in the ESM). The Pt/Ni atomic ratio in the PtNi@CN HNSs was measured to be 68:32, which was in good agreement with the EDX data (70:30) and therefore indicative of the PtNi alloy formation. The detailed Ni 2p XPS spectrum showed the Ni $2p_{3/2}$ peak at 856.00 eV and the Ni $2p_{1/2}$ peak at 873.65 eV (Fig. 1(b)), which corresponds to metallic Ni^0 in the alloy [55]. The Pt 4f XPS spectrum (Fig. 1(c)) contained two components. As observed, the Pt species were predominantly in the metallic state, which effectively provided more active sites for the electrochemical reaction. Meanwhile, the Pt $4f_{7/2}$ binding energy in the PtNi@CN HNSs had a negative shift of approximately 0.12 V as compared to the standard value of bulk Pt, which is ascribed to the electron donation induced by Ni with a smaller electronegativity (Pt: 2.28; Ni: 1.91) [49, 56, 57]. The shift in binding energy also implies the formation of a Pt–Ni alloy.

XRD measurements were performed to investigate the crystalline structure of the PtNi@CN HNSs (Fig. 1(d)). The diffraction peaks of the PtNi@CN HNSs shifted to higher angles than those of pure Pt (JCPDS no. 04-0802), indicating lattice contraction

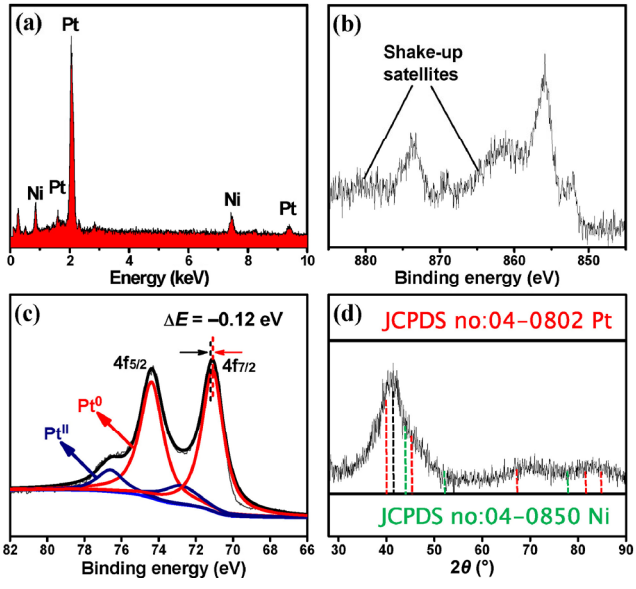

Figure 1 (a) EDX, (b) Ni 2p and (c) Pt 4f XPS, and (d) XRD of PtNi@CN HNSs. The vertical black dotted line in (c) represents the standard value of Pt $4f_{7/2}$.

owing to the substitution of Pt with Ni, which has a smaller atomic radius (Ni = 1.24 Å; Pt = 1.39 Å). The lattice constant of the PtNi alloy nanocrystals with different compositions obeys well Vegard's law (i.e., the linear decrease of the lattice constant with increasing Ni in the Pt matrix) [58]. The alloying Ni content in the PtNi@CN HNSs according to Vegard's law was calculated to be 32 at.% from the (111) peak position of the PtNi@CN HNSs. The atomic fraction of alloyed Ni (32 at.%) was very close to the bulk composition from the EDX measurement (Ni: 30 at.%), which indicates that all Ni atoms entered into the Pt lattice to form a PtNi alloy and demonstrates that the PtNi@CN HNSs had a very high alloying degree. The uniform distribution of Pt^{II} and Ni^{II} species on the cyanogel backbone on the atomic scale facilitated the interaction of the generated Pt and Ni crystal nuclei. Meanwhile, the solid property of the cyanogel effectively restricted the Brownian motion of the generated Pt and Ni crystal nuclei. These two factors were responsible for the high alloying degree of the PtNi@CN HNSs [49–53]. For comparison, PtNi nanoparticles were also synthesized by the $NaBH_4$ reduction method using K_2PtCl_4 and $NiCl_2$ as the reaction precursors. The alloying Ni content in the PtNi nanoparticles was calculated to be only 9.0 at.% according to the XRD data (Fig. S3 in the ESM), which in turn confirms the

fact that the $K_2PtCl_4/K_2Ni(CN)_4$ cyanogel facilitated the formation of the PtNi alloy.

The morphology and structure of the PtNi@CN HNSs were investigated by TEM (Figs. 2(a) and 2(b)). The strong contrast difference between the edge and center gave convincing evidence of the hollow interior [59, 60]. The average diameter of the PtNi@CN HNSs was ca. 20 nm, and the shell thickness was 4–7 nm. For the synthesis of hollow nanostructures, self-templating synthesis, which is the direct synthesis of hollow nanostructures from solid precursors without the need for additional templates, is highly efficient and economical [61, 62]. In our synthesis, the strong stirring played an important role in the formation of the PtNi@CN HNSs because it broke the bulk $K_2PtCl_4/K_2Ni(CN)_4$ cyanogel (Fig. S1 in the ESM) into $K_2PtCl_4/K_2Ni(CN)_4$ cyanogel nanoparticles (Fig. S4 in the ESM). Thus, inside-out Ostwald ripening may have been responsible for the formation of the PtNi@CN HNSs. Specifically, the surface layer of the $K_2PtCl_4/K_2Ni(CN)_4$ cyanogel nanoparticles was initially reduced by $NaBH_4$ to generate a temporary PtNi alloy shell structure. Then, alkaline $NaBH_4$ permeated through the PtNi alloy shell for a further reaction. After reduction, the generated Pt and Ni atoms preferentially deposited on the inner surface of PtNi alloy shell to ultimately form hollow PtNi alloy nanospheres.

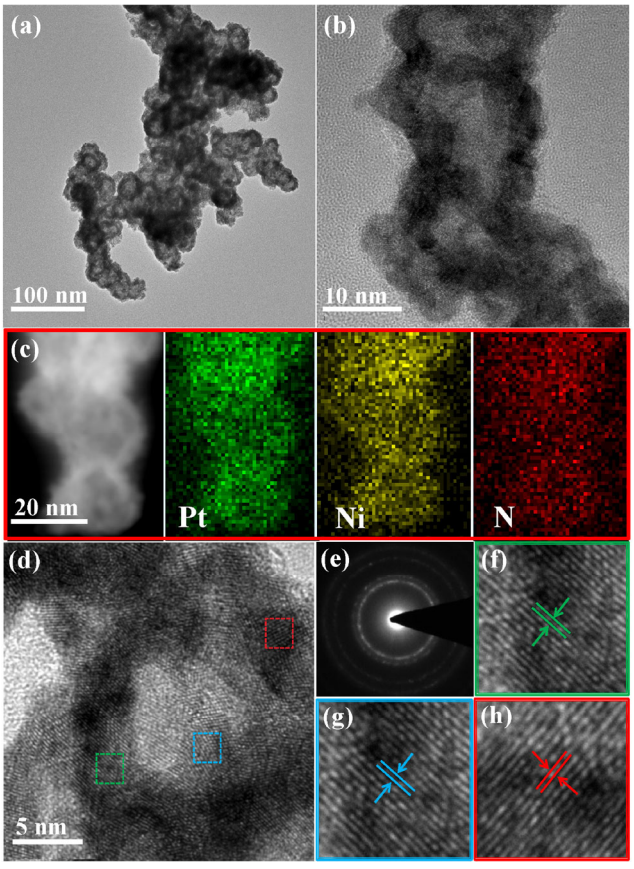

Figure 2 (a) and (b) TEM images of PtNi@CN HNSs. (c) HAADF-STEM image and EDX mapping patterns of Pt, Ni, and N elements. (d) HRTEM image and (e) SAED pattern of PtNi@CN HNSs. (f)–(h) The magnified HRTEM images of the regions marked by red, yellow, and green squares in (d), respectively.

To experimentally visualize the element distribution of the PtNi@CN HNSs, EDX mapping was performed using high-angle annular dark-field scanning TEM (HAADF-STEM). Both the Pt and Ni element patterns were very similar (Fig. 2(c)), further confirming the formation of a PtNi alloy, consistent with the EDX line scanning profiles (Fig. S5 in the ESM). In particular, N was also detected, and its pattern was highly similar to those of Pt and Ni (Fig. 2(c)). Further XPS measurements showed the existence of N (Fig. S6 in the ESM), and the FT-IR spectrum clearly showed the stretching vibration peak of the bridging cyano group at ca. 2,184 cm^{-1} (Fig. S7 in the ESM). Meanwhile, the characteristic N 1s signal was also detected in the XPS spectrum of the single-component Ni nanoparticles (Fig. S8 in the ESM). These experimental results indicate the uniform adsorption of CN^- groups on the PtNi alloy surface. The architecture and surface structure of the PtNi@CN HNSs were further investigated by high-resolution TEM (HRTEM) and selected area electron diffraction (SAED). The HRTEM image (Fig. 2(d)) clearly shows that the PtNi@CN HNSs were composed of many interconnected nanocrystals 2–4 nm in size. Undoubtedly, the small particle size will effectively enhance the utilization of expensive Pt metal. The SAED pattern displays a successive dotted pattern (Fig. 2(e)), thus demonstrating that the PtNi@CN HNSs were polycrystalline. The magnified HRTEM image shows lattice fringes with a spacing of ca. 0.222 nm (Figs. 2(f)–2(h)), corresponding to the Pt{111} facets.

3.2 ORR activity

The electrochemical properties of the PtNi@CN HNSs were first investigated in an acid medium by cyclic

voltammetry (CV) and compared to those of commercial Pt black under the same experimental conditions (Fig. 3(a)). According to the area of the hydrogen desorption peak [47, 48, 63], the electrochemically active surface area (ECSA) of the PtNi@CN HNSs was determined to be 36.4 $m^2 \cdot g_{Pt}^{-1}$, which is bigger than that of commercial Pt black (18.6 $m^2 \cdot g_{Pt}^{-1}$). The hollow structure and small Pt nanocrystal subunits of the PtNi@CN HNSs are believed to be the key reasons for the relatively big ECSA. The higher ECSA for the PtNi@CN HNSs indicates higher Pt utilization, which effectively decreases the cost of cathodic electrocatalysts.

The rotating disk electrode (RDE) technique was used to study the ORR activities of the PtNi@CN HNSs and Pt black by normalizing the current to the geometrical area of the working electrode (Fig. 3(b)). As shown on the ORR polarization curves, the ORR onset (E_{onset}) and half-wave ($E_{1/2}$) potentials of the PtNi@CN HNSs (E_{onset} = 0.948 V; $E_{1/2}$ = 0.86 V) are significantly higher than those of commercial Pt black (E_{onset} = 0.918 V; $E_{1/2}$ = 0.84 V), indicating dramatically improved ORR activity. To further evaluate the intrinsic ORR activity of the electrocatalysts based on the geometrical area of the working electrode, the specific kinetic current density (i_k) of the electrocatalysts for the ORR was calculated by using the Koutecky–Levich (K–L) equation [48, 51]. At a 0.9 V potential, the PtNi@CN HNSs displayed an i_k of 1.71 $mA \cdot cm^{-2}$, which is 1.86 times bigger than that of commercial Pt black (0.92 $mA \cdot cm^{-2}$). Meanwhile, it was found that the i_k of the PtNi@CN HNSs at 0.9 V (1.71 $mA \cdot cm^{-2}$) was also higher than that of various Pt-based nanostructures, including hollow Pt nanostructures (0.529 $mA \cdot cm^{-2}$) [64], porous Pt_1Ni_1 nanostructures (0.307 $mA \cdot cm^{-2}$) [65], Pt–Cu bimetallic nanocrystals (0.84 $mA \cdot cm^{-2}$) [66], and Pt-on-Pd nanostructures (0.67 $mA \cdot cm^{-2}$) [64], further confirming the high ORR activity of the PtNi@CN HNSs. As confirmed by XPS (Fig. 1(c)), XRD (Fig. 1(d)), and TEM (Fig. 2(a)), the shift of the Pt binding energy (i.e., the change of the d-band center), the reduction of the Pt–Pt bond distance, and the particular hollow structure are all responsible for the improved ORR activity of the PtNi@CN HNSs

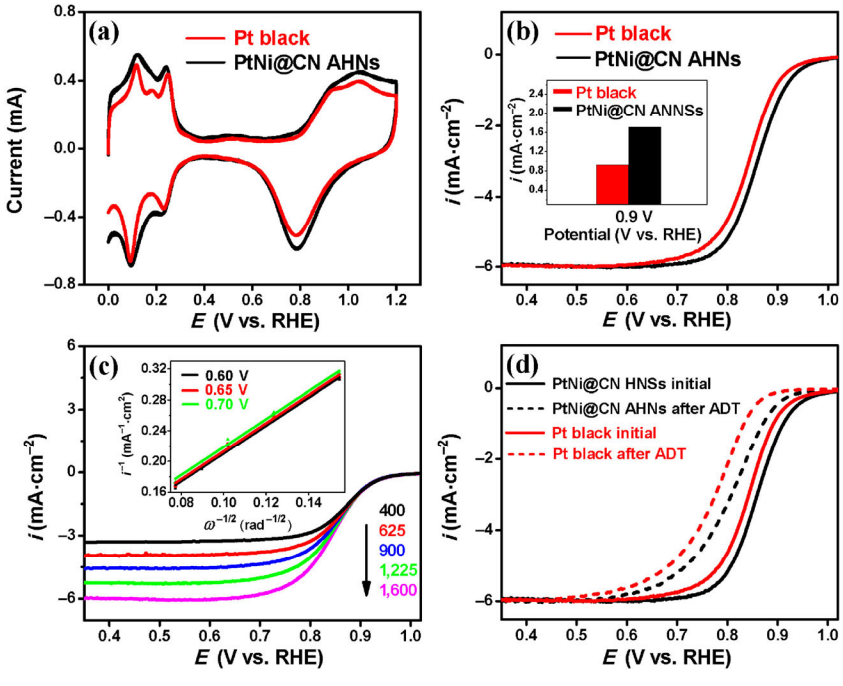

Figure 3 (a) CV curves of the PtNi@CN HNSs and commercial Pt black in a N_2-saturated 0.5 M H_2SO_4 solution at a scan rate of 50 $mV \cdot s^{-1}$. (b) ORR polarization curves of the PtNi@CN HNSs and commercial Pt black in an O_2-saturated 0.5 M H_2SO_4 solution at a scan rate of 5 $mV \cdot s^{-1}$ and a rotation rate of 1,600 rpm. Inset: specific kinetic current densities for the PtNi@CN HNSs and commercial Pt black at 0.90 V. (c) Rotation rate-dependent ORR polarization curves for the PtNi@CN HNSs in O_2-saturated 0.5 M H_2SO_4. Inset: K–L plots for the PtNi@CN HNSs at different potentials. (d) ORR polarization curves of the PtNi@CN HNSs and Pt black after accelerated durability test (ADT).

[11–23, 67–69]. Meanwhile, it is observed that the ORR activity of the PtNi@CN HNSs was better than that of un-functionalized PtNi nanoparticles prepared by the conventional $NaBH_4$ reduction method (Fig. S9 in the ESM). Because CN^- groups on a Pt surface can effectively suppress the adsorption of SO_4^{2-} ions [35, 36], CN^- functionalization also contributed to the improved ORR activity of the PtNi@CN HNSs.

To determine the transferred electron number (n) per O_2 molecule during ORR, the rotation rate-dependent ORR polarization curves were recorded (Fig. 3(c)). As observed, the limited current density increased with increasing rotation rate owing to the enhanced mass transfer of O_2 molecules. The corresponding n was calculated to be 3.86 in the range of 0.60–0.70 V according to the K–L plots (inset in Fig. 3(c)), which demonstrates that the PtNi@CN HNSs had a high electrocatalytic efficiency for the ORR. To investigate the ORR stability of the electrocatalysts, an accelerated durability test (ADT) was carried out by continuous linear potential scans between 0.6 and 1.0 V at 50 $mV \cdot s^{-1}$ in an O_2-saturated H_2SO_4 solution [70]. After 3,000 cycles, the PtNi@CN HNSs and Pt black showed 0.04 and 0.06 V $E_{1/2}$ degradation, respectively (Fig. 3(d)). The smaller $E_{1/2}$ degradation of the PtNi@CN HNSs originated from their lower ECSA loss (Fig. S10 in the ESM). The hollow and interconnected structures of the PtNi@CN HNSs restrained the Ostwald ripening, which improved the ORR stability of the PtNi@CN HNSs.

3.3 ORR selectivity

To evaluate the selectivity of the electrocatalysts, ORR polarization measurements were performed in an O_2-saturated 0.5 M H_2SO_4 solution with and without methanol. The addition of methanol resulted in obvious positive deflection of the ORR polarization curve for both Pt black (Fig. S11 in the ESM) and the un-functionalized PtNi nanoparticles (Fig. 4(a)), in which a big methanol oxidation current was observed between 0.6 and 0.9 V. In comparison, only a small $E_{1/2}$ shift was observed for the ORR polarization curve of the PtNi@CN HNSs after the addition of methanol, and no obvious methanol oxidation current was observed (Fig. 4(b)), indicating that the PtNi@CN HNSs were methanol-tolerant electrocatalysts. The electrocatalytic activity of electrocatalysts for the MOR

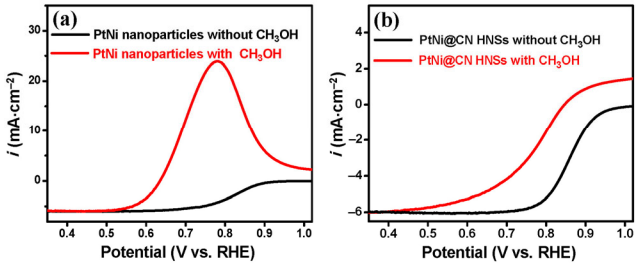

Figure 4 Comparison of ORR polarization curves of (a) un-functionalized PtNi nanoparticles and (b) PtNi@CN HNSs in O_2-saturated 0.5 M H_2SO_4 with and without the presence of 0.25 M methanol at a scan rate of 5 $mV \cdot s^{-1}$ and a rotation rate of 1,600 rpm. PtNi nanoparticles were obtained by conventional $NaBH_4$ reduction, in which K_2PtCl_4 and $NiCl_2$ were used as the reaction precursors.

was investigated by CV in a 0.5 M H_2SO_4 solution containing 0.25 M methanol. It is well known that PtNi alloy electrocatalysts are highly active for the MOR owing to the bifunctional mechanism [26–34]. However, the specific peak current density of the MOR on the PtNi@CN HNSs was much smaller than that on Pt black (Fig. S12 in the ESM) or the un-functionalized PtNi nanoparticles (Fig. 4(a)), confirming the methanol tolerance of the PtNi@CN HNSs. Previous reports have demonstrated that three adjacent Pt sites are necessary for the MOR [71, 72]. As confirmed by the EDX maps (Fig. 3(b)) and XPS measurements (Fig. S6 in the ESM), the CN^- groups were uniformly bound to the PtNi alloy surface. As a result, the contiguous Pt atoms were interrupted by CN^- groups, which restrained the adsorption of methanol onto the Pt surface. The present experimental results clearly demonstrate that chemical functionalization of Pt nanocrystals is indeed an effective approach to improve the methanol tolerance of Pt nanocrystals.

4 Conclusions

In summary, a facile cyanogel reduction method was developed to successfully synthesize PtNi@CN HNSs. As compared to commercial Pt black, the PtNi@CN HNSs displayed significantly improved electrocatalytic activity and durability for the ORR in an acidic medium, which is attributed to their alloying properties and

hollow interconnected structure. More importantly, PtNi@CN HNSs showed good methanol tolerance for the ORR, which originated from the chemical functionalization of the Pt surface. High activity, excellent durability, and particular methanol tolerance make PtNi@CN HNSs promising candidates as cathode electrocatalysts for DMFCs.

Acknowledgements

This research was sponsored by National Natural Science Foundation of China (Nos. 21473111 and 21376122), Natural Science Foundation of Shaanxi Province (No. 2015JM2043), and Fundamental Research Funds for the Central Universities (No. GK201602002).

Electronic Supplementary Material: Supplementary material (digital photograph of $K_2PtCl_4/K_2Ni(CN)_4$ cyanogel, XPS spectrum of PtNi@CN HNSs, XRD pattern of PtNi nanoparticles, N 1s XPS spectrum of PtNi@CN HNSs, ORR polarization curves of PtNi@CN HNSs and PtNi nanoparticles in O_2-saturated 0.5 M H_2SO_4 solution, CVs for PtNi@CN HNSs and commercial Pt black before and after ADT tests, ECSA-normalized CVs of PtNi@CN HNSs and Pt black in N_2-saturated 0.5 M H_2SO_4 + 0.25 M CH_3OH, ORR polarization curves of un-functionalized PtNi nanoparticles in O_2-saturated 0.5 M H_2SO_4 with and without the presence of 0.25 M methanol) is available in the online version of this article at http://dx.doi.org/10.1007/s12274-016-1226-3.

References

[1] Fu, G. T.; Zhang, Q.; Wu, J. Y.; Sun, D. M.; Xu, L.; Tang, Y. W.; Chen, Y. Arginine-mediated synthesis of cube-like platinum nanoassemblies as efficient electrocatalysts. *Nano Res.* **2015**, *8*, 3963–3971.

[2] Yan, H. J.; Meng, M. C.; Wang, L.; Wu, A. P.; Tian, C. G.; Zhao, L.; Fu, H. G. Small-sized tungsten nitride anchoring into a 3D CNT-rGO framework as a superior bifunctional catalyst for the methanol oxidation and oxygen reduction reactions. *Nano Res.* **2016**, *9*, 329–343.

[3] Nassr, A. B. A. A.; Sinev, I.; Pohl, M. M.; Grünert, W.; Bron, M. Rapid microwave-assisted polyol reduction for the preparation of highly active PtNi/CNT electrocatalysts for methanol oxidation. *ACS Catal.* **2014**, *4*, 2449–2462.

[4] Xia, B. Y.; Wu, H. B.; Wang, X.; Lou, X. W. One-pot synthesis of cubic $PtCu_3$ nanocages with enhanced electrocatalytic activity for the methanol oxidation reaction. *J. Am. Chem. Soc.* **2012**, *134*, 13934–13937.

[5] Guo, S. J.; Zhang, S.; Sun, X. L.; Sun, S. H. Synthesis of ultrathin FePtPd nanowires and their use as catalysts for methanol oxidation reaction. *J. Am. Chem. Soc.* **2011**, *133*, 15354–15357.

[6] Huang, H. J.; Wang, X. Recent progress on carbon-based support materials for electrocatalysts of direct methanol fuel cells. *J. Mater. Chem.* A **2014**, *2*, 6266–6291.

[7] Chang, J. F.; Feng, L. G.; Liu, C. P.; Xing, W.; Hu, X. L. Ni_2P enhances the activity and durability of the Pt anode catalyst in direct methanol fuel cells. *Energy Environ. Sci.* **2014**, *7*, 1628–1632.

[8] Tiwari, J. N.; Tiwari, R. N.; Singh, G.; Kim, K. S. Recent progress in the development of anode and cathode catalysts for direct methanol fuel cells. *Nano Energy* **2013**, *2*, 553–578.

[9] Li, L.; Hu, L. P.; Li, J.; Wei, Z. D. Enhanced stability of Pt nanoparticle electrocatalysts for fuel cells. *Nano Res.* **2015**, *8*, 418–440.

[10] Li, Y. J.; Quan, F. X.; Zhu, E. B.; Chen, L.; Huang, Y.; Chen, C. F. Pt_xCu_y nanocrystals with hexa-pod morphology and their electrocatalytic performances towards oxygen reduction reaction. *Nano Res.* **2015**, *8*, 3342–3352.

[11] Baldizzone, C.; Gan, L.; Hodnik, N.; Keeley, G. P.; Kostka, A.; Heggen, M.; Strasser, P.; Mayrhofer, K. J. J. Stability of dealloyed porous Pt/Ni nanoparticles. *ACS Catal.* **2015**, *5*, 5000–5007.

[12] Choi, S.-I.; Shao, M. H.; Lu, N.; Ruditskiy, A.; Peng, H.-C.; Park, J.; Guerrero, S.; Wang, J. G.; Kim, M. J.; Xia, Y. N. Synthesis and characterization of Pd@Pt-Ni core–shell octahedra with high activity toward oxygen reduction. ACS Nano **2014**, *8*, 10363–10371.

[13] Chung, Y. H.; Kim, S. J.; Chung, D. Y.; Lee, M. J.; Jang, J. H.; Sung, Y. E. Tuning the oxygen reduction activity of the Pt-Ni nanoparticles upon specific anion adsorption by varying heat treatment atmospheres. *Phys. Chem. Chem. Phys.* **2014**, *16*, 13726–13732.

[14] Gu, J.; Lan, G. X.; Jiang, Y. Y.; Xu, Y. S.; Zhu, W.; Jin, C. H.; Zhang, Y. W. Shaped Pt-Ni nanocrystals with an ultrathin Pt-enriched shell derived from one-pot hydrothermal synthesis as active electrocatalysts for oxygen reduction. *Nano Res.* **2015**, *8*, 1480–1496.

[15] Kuttiyiel, K. A.; Choi, Y.; Hwang, S. M.; Park, G. G.; Yang, T. H.; Su, D.; Sasaki, K.; Liu, P.; Adzic, R. R. Enhancement of the oxygen reduction on nitride stabilized Pt-M (M = Fe, Co, and Ni) core–shell nanoparticle electrocatalysts. *Nano Energy* **2015**, *13*, 442–449.

[16] Li, M.; Lei, Y. H.; Sheng, N.; Ohtsuka, T. Preparation of low-platinum-content platinum-nickel, platinum-cobalt binary alloy and platinum-nickel-cobalt ternary alloy catalysts for oxygen reduction reaction in polymer electrolyte fuel cells. *J. Power Sources* **2015**, *294*, 420–429.

[17] Sneed, B. T.; Young, A. P.; Jalalpoor, D.; Golden, M. C.; Mao, S. J.; Jiang, Y.; Wang, Y.; Tsung, C. K. Shaped Pd-Ni-Pt core–sandwich–shell nanoparticles: Influence of Ni sandwich layers on catalytic electrooxidations. *ACS Nano* **2014**, *8*, 7239–7250.

[18] Todoroki, N.; Kato, T.; Hayashi, T.; Takahashi, S.; Wadayama, T. Pt-Ni nanoparticle-stacking thin film: Highly active electrocatalysts for oxygen reduction reaction. *ACS Catal.* **2015**, *5*, 2209–2212.

[19] Wu, Y. E.; Wang, D. S.; Niu, Z. Q.; Chen, P. C.; Zhou, G.; Li, Y. D. A strategy for designing a concave Pt-Ni alloy through controllable chemical etching. *Angew. Chem., Int. Ed.* **2012**, *51*, 12524–12528.

[20] Wu, Y. E.; Wang, D. S.; Zhou, G.; Yu, R.; Chen, C.; Li, Y. D. Sophisticated construction of Au islands on Pt-Ni: An ideal trimetallic nanoframe catalyst. *J. Am. Chem. Soc.* **2014**, *136*, 11594–11597.

[21] Xu, X. L.; Zhang, X.; Sun, H.; Yang, Y.; Dai, X. P.; Gao, J. S.; Li, X. Y.; Zhang, P. F.; Wang, H. H.; Yu, N. F. et al. Synthesis of Pt-Ni alloy nanocrystals with high-index facets and enhanced electrocatalytic properties. *Angew. Chem.* **2014**, *126*, 12730–12735.

[22] Zhang, C. L.; Hwang, S. Y.; Peng, Z. M. Size-dependent oxygen reduction property of octahedral Pt-Ni nanoparticle electrocatalysts. *J. Mater. Chem. A* **2014**, *2*, 19778–19787.

[23] Zhang, C. L.; Hwang, S. Y.; Trout, A.; Peng, Z. M. Solid-state chemistry-enabled scalable production of octahedral Pt-Ni alloy electrocatalyst for oxygen reduction Reaction. *J. Am. Chem. Soc.* **2014**, *136*, 7805–7808.

[24] Carpenter, M. K.; Moylan, T. E.; Kukreja, R. S.; Atwan, M. H.; Tessema, M. M. Solvothermal synthesis of platinum alloy nanoparticles for oxygen reduction electrocatalysis. *J. Am. Chem. Soc.* **2012**, *134*, 8535–8542.

[25] Bae, S. J.; Yoo, S. J.; Lim, Y.; Kim, S.; Lim, Y.; Choi, J.; Nahm, K. S.; Hwang, S. J.; Lim, T.-H.; Kim, S.-K. et al. Facile preparation of carbon-supported PtNi hollow nanoparticles with high electrochemical performance. *J. Mater. Chem.* **2012**, *22*, 8820–8825.

[26] Cui, C. H.; Li, H. H.; Yu, S. H. Large scale restructuring of porous Pt-Ni nanoparticle tubes for methanol oxidation: A highly reactive, stable, and restorable fuel cell catalyst. *Chem. Sci.* **2011**, *2*, 1611–1614.

[27] Ding, L. X.; Wang, A.-L.; Li, G.-R.; Liu, Z. Q.; Zhao, W. X.; Su, C. Y.; Tong, Y. X. Porous Pt-Ni-P composite nanotube arrays: Highly electroactive and durable catalysts for methanol electrooxidation. *J. Am. Chem. Soc.* **2012**, *134*, 5730–5733.

[28] Hu, Y. J.; Wu, P.; Yin, Y. J.; Zhang, H.; Cai, C. X. Effects of structure, composition, and carbon support properties on the electrocatalytic activity of Pt-Ni-graphene nanocatalysts for the methanol oxidation. *Appl. Catal. B: Environ.* **2012**, *111–112*, 208–217.

[29] Huang, W. J.; Wang, H. T.; Zhou, J. G.; Wang, J.; Duchesne, P. N.; Muir, D.; Zhang, P.; Han, N.; Zhao, F. P.; Zeng, M. et al. Highly active and durable methanol oxidation electrocatalyst based on the synergy of platinum-nickel hydroxide-graphene. *Nat. Commun.* **2015**, *6*, 10035.

[30] Li, L. H.; Wu, Y. E.; Lu, J.; Nan, C. Y.; Li, Y. D. Synthesis of Pt-Ni/graphene via in situ reduction and its enhanced catalyst activity for methanol oxidation. *Chem. Commun.* **2013**, *49*, 7486–7488.

[31] Liu, X. J.; Cui, C. H.; Gong, M.; Li, H. H.; Xue, Y.; Fan, F. J.; Yu, S. H. Pt-Ni alloyed nanocrystals with controlled architectures for enhanced methanol oxidation. *Chem. Commun.* **2013**, *49*, 8704–8706.

[32] Niu, Z. Q.; Wang, D. S.; Yu, R.; Peng, Q.; Li, Y. D. Highly branched Pt-Ni nanocrystals enclosed by stepped surface for methanol oxidation. *Chem. Sci.* **2012**, *3*, 1925–1929.

[33] Wang, L. L.; Zhang, D. F.; Guo, L. Phase-segregated Pt-Ni chain-like nanohybrids with high electrocatalytic activity towards methanol oxidation reaction. *Nanoscale* **2014**, *6*, 4635–4641.

[34] Ye, S. H.; Feng, J. X.; Wang, A. L.; Xu, H.; Li, G. R. Multi-layered Pt/Ni nanotube arrays with enhanced catalytic performance for methanol electrooxidation. *J. Mater. Chem. A* **2015**, *3*, 23201–23206.

[35] Escudero-Escribano, M.; Zoloff Michoff, M. E.; Leiva, E. P. M.; Marković, N. M.; Gutiérrez, C.; Cuesta, Á. Quantitative study of non-covalent interactions at the electrode–electrolyte interface using cyanide-modified Pt(111) electrodes. *Chemphyschem* **2011**, *12*, 2230–2234.

[36] Strmcnik, D.; Escudero-Escribano, M.; Kodama, K.; Stamenkovic, V. R.; Cuesta, A.; Marković, N. M. Enhanced electrocatalysis of the oxygen reduction reaction based on patterning of platinum surfaces with cyanide. *Nat. Chem.* **2010**, *2*, 880–885.

[37] Genorio, B.; Strmcnik, D.; Subbaraman, R.; Tripkovic, D.; Karapetrov, G.; Stamenkovic, V. R.; Pejovnik, S.; Marković, N. M. Selective catalysts for the hydrogen oxidation and oxygen reduction reactions by patterning of platinum with calix[4]arene molecules. *Nat. Mater.* **2010**, *9*, 998–1003.

[38] Genorio, B.; Subbaraman, R.; Strmcnik, D.; Tripkovic, D.; Stamenkovic, V. R.; Markovic, N. M. Tailoring the selectivity and stability of chemically modified platinum nanocatalysts

to design highly durable anodes for PEM fuel cells. *Angew. Chem., Int. Ed.* **2011**, *50*, 5468–5472.

[39] Tong, Y. J. Unconventional promoters of catalytic activity in electrocatalysis. *Chem. Soc. Rev.* **2012**, *41*, 8195–8209.

[40] Makosch, M.; Lin, W. I.; Bumbálek, V.; Sá, J.; Medlin, J. W.; Hungerbühler, K.; van Bokhoven, J. A. Organic thiol modified Pt/TiO_2 catalysts to control chemoselective hydrogenation of substituted nitroarenes. *ACS Catal.* **2012**, *2*, 2079–2081.

[41] Marshall, S. T.; O'Brien, M.; Oetter, B.; Corpuz, A.; Richards, R. M.; Schwartz, D. K.; Medlin, J. W. Controlled selectivity for palladium catalysts using self-assembled monolayers. *Nat. Mater.* **2010**, *9*, 853–858.

[42] Kwon, S. G.; Krylova, G.; Sumer, A.; Schwartz, M. M.; Bunel, E. E.; Marshall, C. L.; Chattopadhyay, S.; Lee, B.; Jellinek, J.; Shevchenko, E. V. Capping ligands as selectivity switchers in hydrogenation reactions. *Nano Lett.* **2012**, *12*, 5382–5388.

[43] Ren, D.; He, L.; Yu, L.; Ding, R. S.; Liu, Y. M.; Cao, Y.; He, H. Y.; Fan, K. N. An unusual chemoselective hydrogenation of quinoline compounds using supported gold catalysts. *J. Am. Chem. Soc.* **2012**, *134*, 17592–17598.

[44] Tan, Y. M.; Xu, C. F.; Chen, G. X.; Zheng, N. F.; Xie, Q. J. A graphene-platinum nanoparticles-ionic liquid composite catalyst for methanol-tolerant oxygen reduction reaction. *Energy Environ. Sci.* **2012**, *5*, 6923–6927.

[45] Snyder, J.; Fujita, T.; Chen, M. W.; Erlebacher, J. Oxygen reduction in nanoporous metal–ionic liquid composite electrocatalysts. *Nat. Mater.* **2010**, *9*, 904–907.

[46] Xu, G. R.; Han, S. H.; Liu, Z. H.; Chen Y. The chemical functionalized platinum nanodendrites: The effect of chemical molecular weight on electrocatalytic property. *J. Power Sources* **2016**, *306*, 587–592.

[47] Li, F. M.; Gao, X. Q.; Li, S. N.; Chen, Y.; Lee, J. M. Thermal decomposition synthesis of functionalized PdPt alloy nanodendrites with high selectivity for oxygen reduction reaction. *NPG Asia Mater.* **2015**, *7*, e219.

[48] Fu, G. T.; Jiang, X.; Gong, M. X.; Chen, Y.; Tang, Y. W.; Lin, J.; Lu, T. H. Highly branched platinum nanolance assemblies by polyallylamine functionalization as superior active, stable, and alcohol-tolerant oxygen reduction electrocatalysts. *Nanoscale* **2014**, *6*, 8226–8234.

[49] Liu, X. Y.; Xu, G. R.; Chen, Y.; Lu, T. H.; Tang, Y. W.; Xing, W. A strategy for fabricating porous PdNi@Pt core–shell nanostructures and their enhanced activity and durability for the methanol electrooxidation. *Sci. Rep.* **2015**, *5*, 7619.

[50] Zhang, L.; Lu, D. K.; Chen, Y.; Tang, Y. W.; Lu, T. H. Facile synthesis of Pd-Co-P ternary alloy network nanostructures and their enhanced electrocatalytic activity towards hydrazine oxidation. *J. Mater. Chem. A* **2014**, *2*, 1252–1256.

[51] Liu, X. Y.; Fu, G. T.; Chen, Y.; Tang, Y. W.; She, P. L.; Lu, T. H. Pt-Pd-Co trimetallic alloy network nanostructures with superior electrocatalytic activity towards the oxygen reduction reaction. *Chem.—Eur. J.* **2014**, *20*, 585–590.

[52] Zhang, L.; Wan, L.; Ma, Y. R.; Chen, Y.; Zhou, Y. M.; Tang, Y. W.; Lu, T. H. Crystalline palladium–cobalt alloy nanoassemblies with enhanced activity and stability for the formic acid oxidation reaction. *Appl. Catal. B: Environ.* **2013**, *138–139*, 229–235.

[53] Xu, J. F.; Liu, X. Y.; Chen, Y.; Zhou, Y. M.; Lu, T. H.; Tang, Y. W. Platinum-cobalt alloy networks for methanol oxidation electrocatalysis. *J. Mater. Chem.* **2012**, *22*, 23659–23667.

[54] Garsany, Y.; Baturina, O. A.; Swider-Lyons, K. E.; Kocha, S. S. Experimental methods for quantifying the activity of platinum electrocatalysts for the oxygen reduction reaction. *Anal. Chem.* **2010**, *82*, 6321–6328.

[55] Chen, L. Y.; Guo, H.; Fujita, T.; Hirata, A.; Zhang, W.; Inoue, A.; Chen, M. W. Nanoporous PdNi bimetallic catalyst with enhanced electrocatalytic performances for electrooxidation and oxygen reduction reactions. *Adv. Funct. Mater.* **2011**, *21*, 4364–4370.

[56] Yang, J.; Zhou, W.; Cheng, C. H.; Lee, J. Y.; Liu, Z. Pt-decorated PdFe nanoparticles as methanol-tolerant oxygen reduction electrocatalyst. *ACS Appl. Mater. Interfaces* **2010**, *2*, 119–126.

[57] Zhang, G.; Shao, Z. G.; Lu, W. T.; Xiao, H.; Xie, F.; Qin, X. P.; Li, J.; Liu, F. Q.; Yi, B. L. Aqueous-phase synthesis of sub 10 nm $Pd_{core}@Pt_{shell}$ nanocatalysts for oxygen reduction reaction using amphiphilic triblock copolymers as the reductant and capping agent. The *J. Phys. Chem. C* **2013**, *117*, 13413–13423.

[58] Hsieh, C. T.; Yu, P.-Y.; Tzou, D. Y.; Hsu, J.-P.; Chiu, Y. R. Bimetallic Pd–Rh nanoparticles onto reduced graphene oxide nanosheets as electrocatalysts for methanol oxidation. *J. Electroanal. Chem.* **2016**, *761*, 28–36.

[59] Li, T.; You, H.; Xu, M. W.; Song, X. P.; Fang, J. X. Electrocatalytic properties of hollow coral-like platinum mesocrystals. *ACS Appl. Mater. Interfaces* **2012**, *4*, 6942–6948.

[60] Li, C. L.; Jiang, B.; Imura, M.; Malgras, V.; Yamauchi, Y. Mesoporous Pt hollow cubes with controlled shell thicknesses and investigation of their electrocatalytic performance. *Chem. Commun.* **2014**, *50*, 15337–15340.

[61] Wang, X. J.; Feng, J.; Bai, Y. C.; Zhang, Q.; Yin, Y. D. Synthesis, properties, and applications of hollow micro-/nanostructures. *Chem. Rev.*, in press, DOI: 10.1021/acs.chemrev.5b00731.

[62] Li, Y. S.; Shi, J. L. Hollow-structured mesoporous materials:

Chemical synthesis, functionalization and applications. *Adv. Mater.* **2014**, *26*, 3176–3205.

[63] Fu, G. T.; Wu, K.; Lin, J.; Tang, Y. W.; Chen, Y.; Zhou, Y. M.; Lu, T. H. One-pot water-based synthesis of Pt–Pd alloy nanoflowers and their superior electrocatalytic activity for the oxygen reduction reaction and remarkable methanol-tolerant ability in acid media. *J. Phys. Chem. C* **2013**, *117*, 9826–9834.

[64] Peng, Z. M.; Wu, J. B.; Yang, H. Synthesis and oxygen reduction electrocatalytic property of platinum hollow and platinum-on-silver nanoparticles. *Chem. Mater.* **2010**, *22*, 1098–1106.

[65] Wang, R. Y.; Xu, C. X.; Bi, X. X.; Ding, Y. Nanoporous surface alloys as highly active and durable oxygen reduction reaction electrocatalysts. *Energy Environ. Sci.* **2012**, *5*, 5281–5286.

[66] Zhu, C. M.; Gao, A.; Wang, Y.; Liu, Y. Pt–Cu bimetallic electrocatalysts with enhanced catalytic properties for oxygen reduction. *Chem. Commun.* **2014**, *50*, 13889–13892.

[67] Bae, J. H.; Han, J. H.; Chung, T. D. Electrochemistry at nanoporous interfaces: New opportunity for electrocatalysis. *Phys. Chem. Chem. Phys.* **2012**, *14*, 448–463.

[68] Chen, C.; Kang, Y. J.; Huo, Z. Y.; Zhu, Z. W.; Huang, W. Y.; Xin, H. L.; Snyder, J. D.; Li, D. G.; Herron, J. A.; Mavrikakis, M. et al. Highly crystalline multimetallic nanoframes with three-dimensional electrocatalytic surfaces. *Science* **2014**, *343*, 1339–1343.

[69] Dubau, L.; Asset, T.; Chattot, R.; Bonnaud, C.; Vanpeene, V.; Nelayah, J.; Maillard, F. Tuning the performance and the stability of porous hollow PtNi/C nanostructures for the oxygen reduction reaction. *ACS Catal.* **2015**, *5*, 5333–5341.

[70] Zhu, J. B.; Xiao, M. L.; Zhao, X.; Liu, C. P.; Ge, J. J.; Xing, W. Strongly coupled Pt nanotubes/N-doped graphene as highly active and durable electrocatalysts for oxygen reduction reaction. *Nano Energy* **2015**, *13*, 318–326.

[71] Salgado, J. R. C.; Antolini, E.; Gonzalez, E. R. Carbon supported Pt–Co alloys as methanol-resistant oxygen-reduction electrocatalysts for direct methanol fuel cells. *Appl. Catal. B: Environ.* **2005**, *57*, 283–290.

[72] Kamiya, K.; Kamai, R.; Hashimoto, K.; Nakanishi, S. Platinum-modified covalent triazine frameworks hybridized with carbon nanoparticles as methanol-tolerant oxygen reduction electrocatalysts. *Nat. Commun.* **2014**, *5*, 5040.